

Helium ion irradiation enhanced precipitation and the impact on cavity formation in a HfNbZrTi refractory high entropy alloy

D. Li^a, N. Jia^a, H. Huang^b, S. Chen^a, Y. Dou^c, X. He^c, W. Yang^c, Y. Xue^a, Z. Hua^d, F. Zhang^d, L. Wang^a, K. Jin^{a,e,*}, H. Cai^a

^a School of Materials Science and Engineering, Beijing Institute of Technology, Beijing, China

^b Shanghai Institute of Applied Physics, Chinese Academy of Sciences, Shanghai, China

^c China Institute of atomic energy, Beijing, China

^d Analytical and Testing Center, Beijing Institute of Technology, Beijing, China

^e Advanced Research Institute of Multidisciplinary Science, Beijing Institute of Technology, Beijing, China



ARTICLE INFO

Article history:

Received 1 March 2021

Revised 31 March 2021

Accepted 17 April 2021

Available online 23 April 2021

Keywords:

Refractory high entropy alloy

Ion irradiation

Cavity

Radiation enhanced precipitation

ABSTRACT

Refractory high entropy alloys have gained increasing research attention on their irradiation response for the potential applications in nuclear engineering. Considering the metastable nature of their single-phase solid solution structures, the phase stability under irradiation, especially at elevated temperatures, should be a critical concern during the long-term service. In the present study, a typical refractory high entropy alloy with a single-phase body-centered cubic (BCC) structure, HfNbZrTi, is irradiated with 1.5 MeV He ions under 700 °C to various fluences from 5×10^{15} to $1 \times 10^{17} \text{ cm}^{-2}$. Significant irradiation-enhanced precipitation with Hf and Zr enrichment is observed. Although most extended precipitates with tens of nanometers in size are with a hexagonal close-packed (HCP) structure, different structures, including HCP, face-centered cubic (FCC), and the close-packed structures containing highly mixed stacking sequences, are observed in the small precipitates with a few nanometers in size formed at the early-stage precipitation process, suggesting various precipitation paths. By carefully examining the interfaces between the matrix and precipitates, the precipitation mechanism is discussed with similar but slightly different orientation relationships from the Burgers path. Such irradiation-enhanced precipitation process has a strong impact on the cavity formation in this alloy. The cavities are dominantly formed through the heterogeneous nucleation and growth mechanisms, accompanied by the precipitation process. The cavities with low densities but large sizes are observed to be highly clustered with the precipitates. These findings not only unveil the detailed precipitation behavior in a model refractory high entropy alloy under irradiation, but also highlight the critical role that the phase stability plays on the irradiation damage of this novel alloy system.

© 2021 Elsevier B.V. All rights reserved.

1. Introduction

The development of novel structural materials with outstanding properties under extreme environments is critical to the next-generation nuclear power plants [1]. Recent findings on the enhanced mechanical properties and radiation resistance in single-phase concentrated solid solution alloys (SP-CSAs), including high entropy alloys (HEAs) [2,3], have attracted increasing attention from the nuclear materials community [4,5]. In order to understand the mechanism of radiation resistance of this new family of alloys and to evaluate their application potential in nuclear indus-

try, a number of investigations have been performed on the microstructural evolution under ion irradiation at both room temperature and elevated temperatures [6–14]. Overall speaking, the irradiation induced dislocation loop growth, void swelling, and He bubble formation have been observed to be suppressed or delayed with increasing compositional complexity, which has mainly been attributed to the severe chemical disorder, lattice distortion, and the resulting unique energy dissipation and defect kinetic properties [15–17].

Other than irradiation defects, the irradiation induced (or enhanced) phase instability is an important concern for the application of alloys in nuclear engineering. This issue deserves a special concern for HEAs, since their single-phase solid solution phases are usually thermally metastable [18]. For example, although heavy ion radiation-induced segregation (RIS) has been reported to be

* Corresponding author.

E-mail address: jinke@bit.edu.cn (K. Jin).

suppressed in several NiCoFeCr-based 3-d transition metal HEAs [6,19], decompositions with secondary phase formation have been observed in NiCoFeCrMn and NiCoFeCrPd under electron irradiations [20] and in NiCoFeCrAl_{0.12} under ion irradiation [21]. Other than in the 3d transition-metal HEAs, phase separation has also frequently occurred in the refractory high entropy alloys (RHEAs) under elevated temperatures, with or even without irradiations, such as the precipitates formation in NbTiVZr_x at 700 °C and the Cr- and V-enriched second-phase particles formed in WTaCrV at 800 °C [22,23].

Precipitates or precipitate-matrix interfaces are double-edged swords for irradiation-induced defect evolution, such as the nucleation and growth of voids and bubbles [24–26]. On one hand, they can act as the recombination centers for vacancy-interstitial annihilation to limit the oversaturation of defect concentration to suppress the formation and growth of voids and bubbles in, e.g., oxide-dispersion-strengthened (ODS) alloys [27]. On the other hand, the interfaces, especially those incoherent interfaces, can act as defect collectors where the defects can accumulate and nucleate [25]. Therefore, it is untrivial to judge whether the irradiation-induced precipitation is beneficial or catastrophic to the overall irradiation resistance, which demands careful studies on the nature of precipitates and precipitation process.

While majority of existing studies on the irradiation effects of SP-CSAs have been focused on the face-centered cubic (FCC) structured NiCoFeCr-based alloys, increasing research interests have been targeted on the body-centered cubic (BCC) structured RHEAs, due to their outstanding mechanical properties at high temperatures, relatively lower neutron cross-sections, and possible high resistance to irradiation swelling [22,23,28–30]. HfNbZrTi is a single-phase BCC structured RHEA with outstanding mechanical properties [31,32]. This alloy and the derivative HfNbZrTi-based alloys have formed a large group of RHEAs that have received extensive studies [18,33,34]. In this work, the homogenized HfNbZrTi alloy,

as a typical single-phase RHEA, is irradiated with He ions at 700 °C to various fluences. The irradiation-enhanced precipitation behavior and the impact on He bubble formation are studied. Furthermore, the necessity of attention to the phase stability is emphasized for the RHEAs under irradiation at elevated temperatures.

2. Experimental

The raw metals of Hf, Nb, Zr, and Ti with purities higher than 99.95 wt.% were carefully weighted equiatomicly, and then melted using induction levitation melting under argon atmosphere. The as-cast ingots were cut into slabs with 12 mm thickness, which were subsequently cold-rolled to 50% thickness reduction, annealed at 1300 °C for 24 h, and water quenched, in order to achieve homogenized elemental distribution and large grain size to simplify the following analyses. The crystal structure from the X-ray diffraction (XRD) pattern, microstructure from the scanning electron microscopy (SEM)-backscattered electron (BSE) image, and the atomic-scale structure from scanning transmission electron microscopy (STEM) high-angle annular dark-field (HAADF) image are shown in Fig. 1(a–c). A single-phase BCC solid-solution structure is demonstrated, which is consistent with the previous characterizations for the homogenized HfNbZrTi alloy [31].

The 1.5 MeV He ion irradiations were performed using a 4 MV Pelletron accelerator at the Shanghai Institute of Applied Physics, Chinese Academy of Sciences (SINAP-CAS). The samples were irradiated to four fluences of 5×10^{15} , 2×10^{16} , 5×10^{16} , and $1 \times 10^{17} \text{ cm}^{-2}$, with a constant flux of $1.25 \times 10^{12} \text{ ion/cm}^2/\text{s}$. 700 °C was selected as the irradiation temperature since it is within the common service temperature regime for the in-core structure materials in several Gen IV reactors, such as the lead fast reactors [35]. Moreover, as mentioned in the Introduction section, the structural stability under irradiation is a critical issue in this temperature regime and deserves special attention. The displacement and

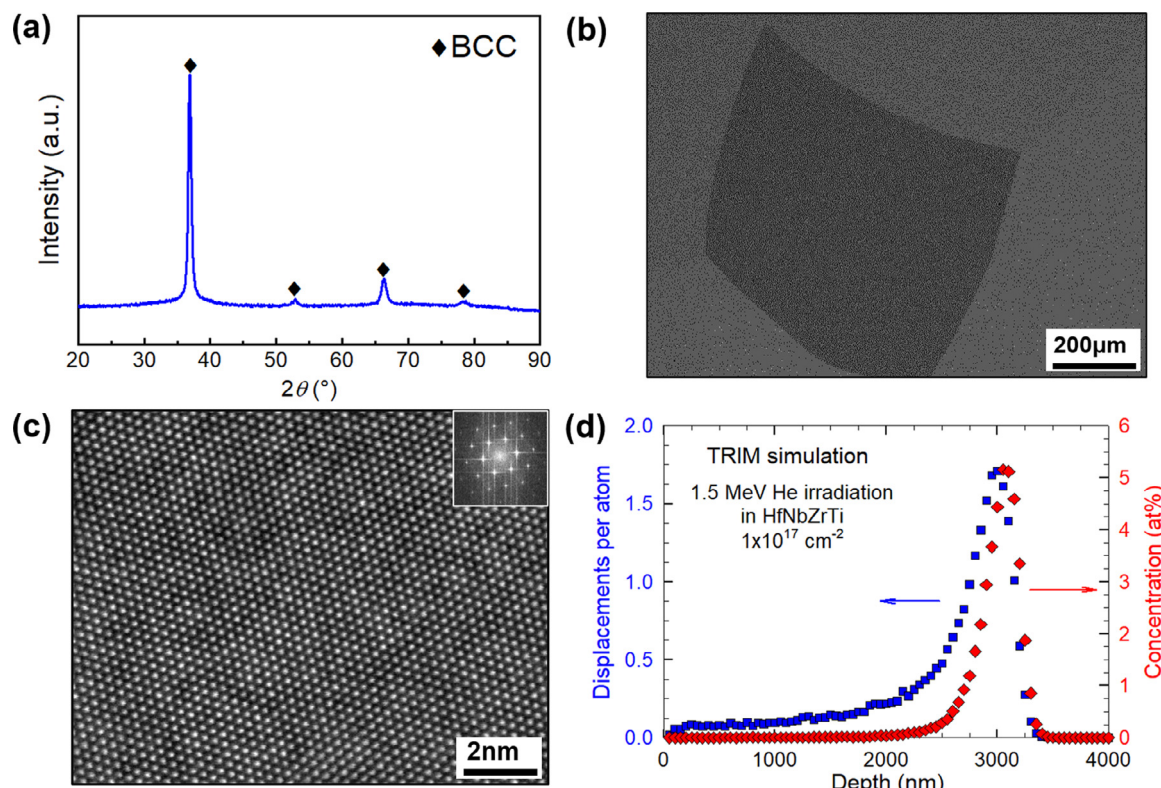


Fig. 1. The (a) XRD, (b) SEM-BSE, and (c) STEM-HAADF characterizations of the as-prepared HfNbZrTi samples. (d) shows the SRIM/TRIM prediction of the displacement and implanted ion profiles of the He ion irradiation in HfNbZrTi under the fluence of $1 \times 10^{17} \text{ cm}^{-2}$.

implanted He ion profiles, as shown in Fig. 1(d) for the case of the highest irradiation fluence, were simulated using the Stopping and Range of Ions in Matter (SRIM) code [36], under the Kinchin-Pease mode. The threshold displacement energies were assumed as 30, 40, 78, and 61 eV, for Ti, Zr, Nb, and Hf elements, respectively, to maintain consistent with the literature [37].

The cross-sectional TEM samples were taken out from the near center positions of the irradiated samples using the focused ion beam (FIB, FEI-Helios G4) lift-out techniques. Up to 30 keV Ga ions were used for trenching and thinning the samples, while 1 keV Ga ions were used for the final cleaning to minimize the FIB damage. A double Cs-corrected Themis Z STEM operated at 300 keV and a probe Cs-corrected Themis Z STEM operated at 200 keV, both equipped with Super-X EDX (energy dispersive X-ray) detectors, were employed for microstructural imaging and elemental mapping.

3. Results and discussions

The STEM-HAADF images shown in Fig. 2 overview the microstructures near the damage/He peak regions for the four irradiation fluences. The cavities (likely He bubbles due to the He ion implantation) are observed in all the samples, but the density is considerably low, especially in the low fluence regime. For example, under irradiation to the lowest fluence of $5 \times 10^{15} \text{ cm}^{-2}$, only one cavity is found in such a large area (see also Fig. S1a for a low-mag TEM image with an area of $3.5 \times 3.5 \mu\text{m}^2$ with only one cavity observed). With increasing fluence till $\sim 5 \times 10^{16} \text{ cm}^{-2}$, more cavities are formed with generally uniform distributions. When the irradiation fluence reaches $1 \times 10^{17} \text{ cm}^{-2}$, the cavities are no longer isolated/scattered but highly clustered, while large precipitates with the scale of tens of nanometers can be clearly observed near the damage peak regime.

Fig. 3(a-d) show the defect images at higher magnifications. It is clear that all the observed cavities are formed at the precipitates regardless of the irradiation fluence. The EDS mappings shown in Fig. 3(e-g) demonstrate that the precipitates are in general Hf and Zr enriched while Nb and Ti depleted. Moreover, the average sizes (diameters) of the cavities are ~29, 27, 26, and 29 nm for the four (from low to high) fluences (See Fig. S2 for the size distribution statistics), showing insignificant variance in the average cavity size

with increasing fluence. Further considering the low cavity density as noted above, our findings demonstrate that the cavity formation mechanism is not homogeneous nucleation, but heterogeneous nucleation accompanied with the precipitation process.

It should be noticed that both the cavities and precipitates are mainly formed in the peak irradiation regions. They are not observed in the unirradiated (deeper) regions, and are rarely observed in the low dose (shallow/surface) regions, even with the highest fluence irradiation (see Fig. 1 and Fig. S1b). Therefore, the precipitation is not solely due to the thermal effect, but an irradiation induced or enhanced process [21]. On the other hand, similar to the majority of refractory high entropy alloys, the single-phase BCC structure is a thermally metastable phase of HfNbZrTi. It has been shown that the Hf-Zr enriched secondary phase can indeed form under thermal annealing in the temperature regime between 550 to 800 °C [38], and the precipitates are more easily to be formed near the defective regions such as grain boundaries (See Fig. S3). From the thermodynamic perspective, the driving force of phase separation in our case is the large formation enthalpy, which is mainly attributed to (1) the severe lattice distortion between the larger Hf ($r= 1.54 \text{ \AA}$) and Zr ($r= 1.55 \text{ \AA}$) atoms and the smaller Nb ($r= 1.43 \text{ \AA}$) and Ti ($r= 1.43 \text{ \AA}$) atoms [39], and (2) the large positive mixing enthalpy between Nb and Hf / Zr (4 / 4 kJ/mol) [40,41]. Therefore, the formation of Hf-Zr enriched precipitates in the irradiation damage peak regions could reasonably be regarded as the radiation-enhanced precipitation (REP). The He-ion irradiation at elevated temperatures have been demonstrated to cause active defect migration in BCC metals [42,43]; such enhanced atomic diffusion is likely to overcome the kinetic barriers of second phase formation and cause the REP [21,24]. Compared with other RHEAs without significant REP under similar irradiation conditions, e.g. TiVNbTa, in which the He bubbles are much smaller (~8 nm in diameter at the irradiation fluence of $1 \times 10^{17} \text{ cm}^{-2}$) and are uniformly distributed [44], the REP induced clustering of large He cavities in HfNbZrTi is detrimental to the overall irradiation resistance.

Since the irradiation enhanced precipitation in HfNbZrTi is a core process during the microstructural evolution under irradiation, it is necessary to understand in-depth the precipitation process and the corresponding mechanism. Therefore, careful characterizations on the structure of precipitates, especially during their

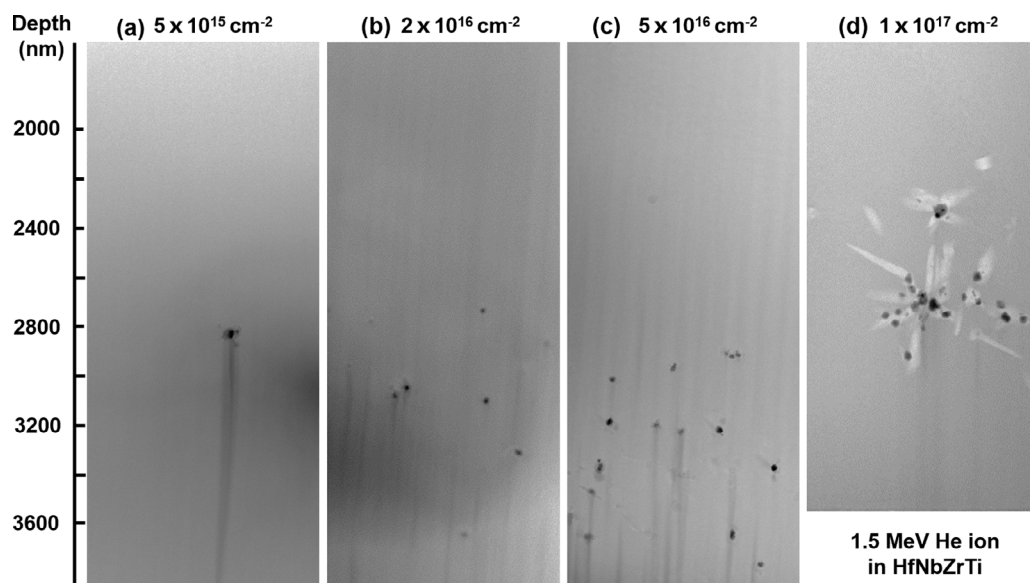


Fig. 2. Low-mag STEM-HAADF images overviewing of the damage/He peak region for different irradiation fluences. The curtaining artificial appears during the FIB sample preparation process.

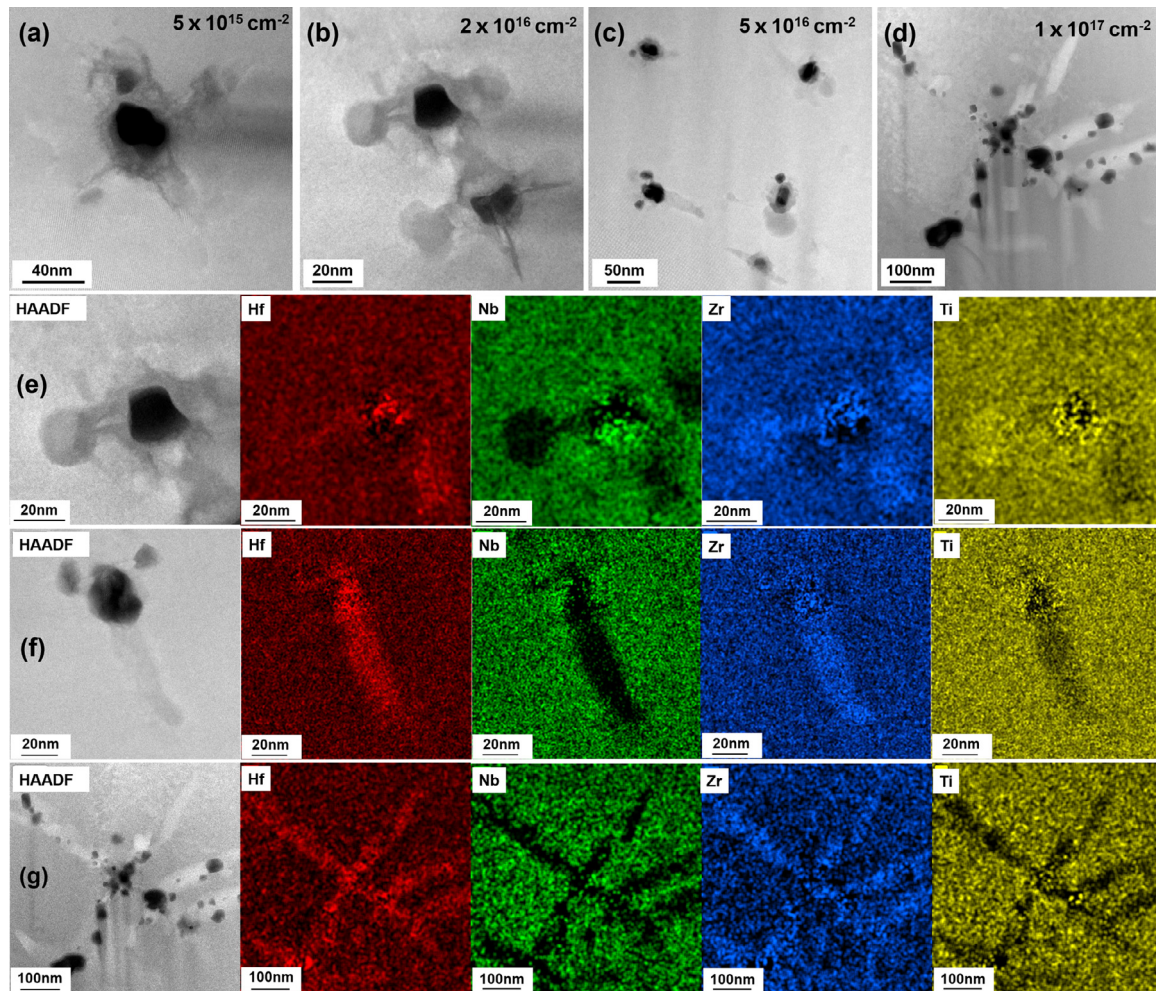


Fig. 3. (a-d) STEM-HAADF images of the cavities and precipitates at different irradiation fluences. (e-g) show the elemental distribution near the defects for 2×10^{16} , 5×10^{16} , and $1 \times 10^{17} \text{ cm}^{-2}$, respectively.

initial formation stage, are performed. To begin with, the microstructures of the well-grown precipitates observed in the samples irradiated to the highest two fluences, 5×10^{16} and $1 \times 10^{17} \text{ cm}^{-2}$, are shown in Fig. 4. Such plate-like precipitates are over 100 nm in length and tens of nanometers in width. The atomic-scale images observed from both $<100>_{\text{BCC}}$ (Fig. 4a, b) and $<311>_{\text{BCC}}$ (Fig. 4c-f) directions of the BCC matrix demonstrate the well-organized HCP structures, along the $<110>_{\text{HCP}}$ and $<111>_{\text{HCP}}$ directions, respectively, of the precipitates, indicating HCP as the "stabled" crystal structure of precipitates, which is consistent with the previous observation [38] on the precipitates formed during thermal annealing.

In order to understand the initial precipitation stage, the microstructure of precipitates with much smaller size or at the samples irradiated to lower fluences are characterized, as shown in Figs. 5–7. It is very interesting to find that the precipitates formed at the early stage of the precipitation process are not necessarily in HCP structures. For example, Fig. 5 shows a precipitate with ~3 nm width, which is no longer HCP structured but FCC structured with a $<110>_{\text{FCC}}$ direction parallel to the electron beam. Together with the EDS mappings shown in Fig. 5(c), this finding demonstrates a metastable FCC-structured Hf-Zr phase that can form at the early precipitation stage during high-temperature irradiation.

In fact, such FCC structured Hf-Zr phases are commonly observed in this work, for those precipitates smaller than 10 nm. However, most of them are not perfectly stacked but contain a number of stacking faults. As shown in Fig. 6(b, e), and the region

"II" of (f), two stacking faults are observed in the marked regions with an overall FCC structure. For example, the local stacking sequence marked in Fig. 6(b) is "ABCABC|BCA|CABCAB". Such stacking faults are likely formed to mitigate the strain between the matrix and precipitates, as will be discussed below. Other than the stacking faults, grain boundaries are also frequently observed in precipitates. For example, as shown in Fig. 6(f), the two FCC regions, I and II, are separated by a defective region with ~1 nm width.

Moreover, many precipitates contain multiple phases and grains with only a few nanometers in size. As shown in Fig. 7, at least three HCP structured grains (H1-H3), two FCC structured grains (F1, F2), as well as a grain with mixed stacking sequence (M1) are observed in a small area of $\sim 15 \times 15 \text{ nm}^2$ in size. As shown in Fig. 7(c), the M1 grain forms a stacking sequence of "ABCAB|ABC|BC|BCAB|AB", which could either be regarded as an FCC structured grain with an extremely high density of stacking faults, or a highly mixed FCC and HCP structured nanolayers. Here it should be noticed that the difference in the interlayer separation between the stacking sequences is not observed beyond the experimental uncertainties, and therefore the interatomic distances can reasonably be assumed to maintain the same between the FCC and HCP phases.

Such small sizes of the grains/phases introduce high density of grain boundaries and phase boundaries, including both coherent boundaries, e.g., between H2 and F2, and incoherent boundaries, e.g., between M1, H2, and H3 in Fig. 7(b). These boundaries,

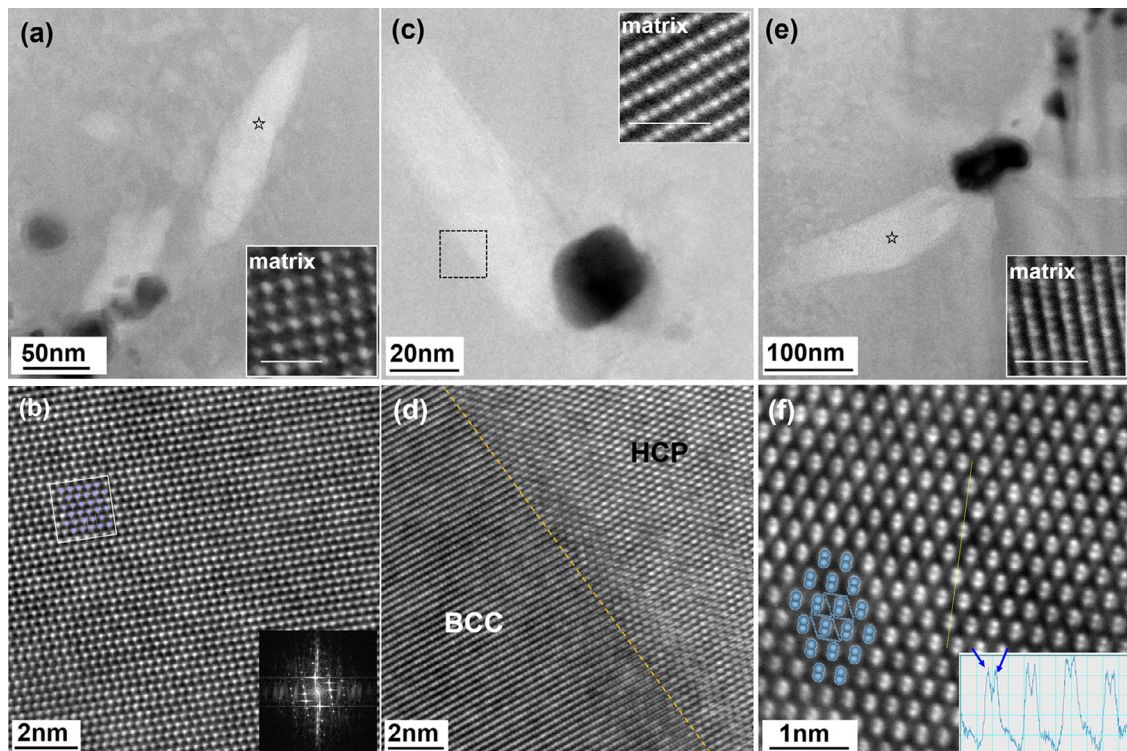


Fig. 4. STEM-HAADF images showing the (a, c, e) microstructures and (b, d, f) atomic-scale structures of the well-grown precipitates; (a, b) for a precipitate formed under $1 \times 10^{17} \text{ cm}^{-2}$ irradiation through $<100>_{\text{BCC-matrix}}$; (c, d) for a precipitate formed under $5 \times 10^{16} \text{ cm}^{-2}$ irradiation through $<311>_{\text{BCC-matrix}}$; (e, f) for a precipitate formed under $1 \times 10^{17} \text{ cm}^{-2}$ irradiation through $<311>_{\text{BCC-matrix}}$. The stars shown in (a) and (e) indicate the approximate image positions of (b) and (f), respectively. The overlayed colored balls in (b, f) are the atomic structure models for $\{110\}_{\text{HCP}}$ and $\{111\}_{\text{HCP}}$ planes, respectively. The line scan in (f) demonstrates the separated atoms corresponding to the atomic model.

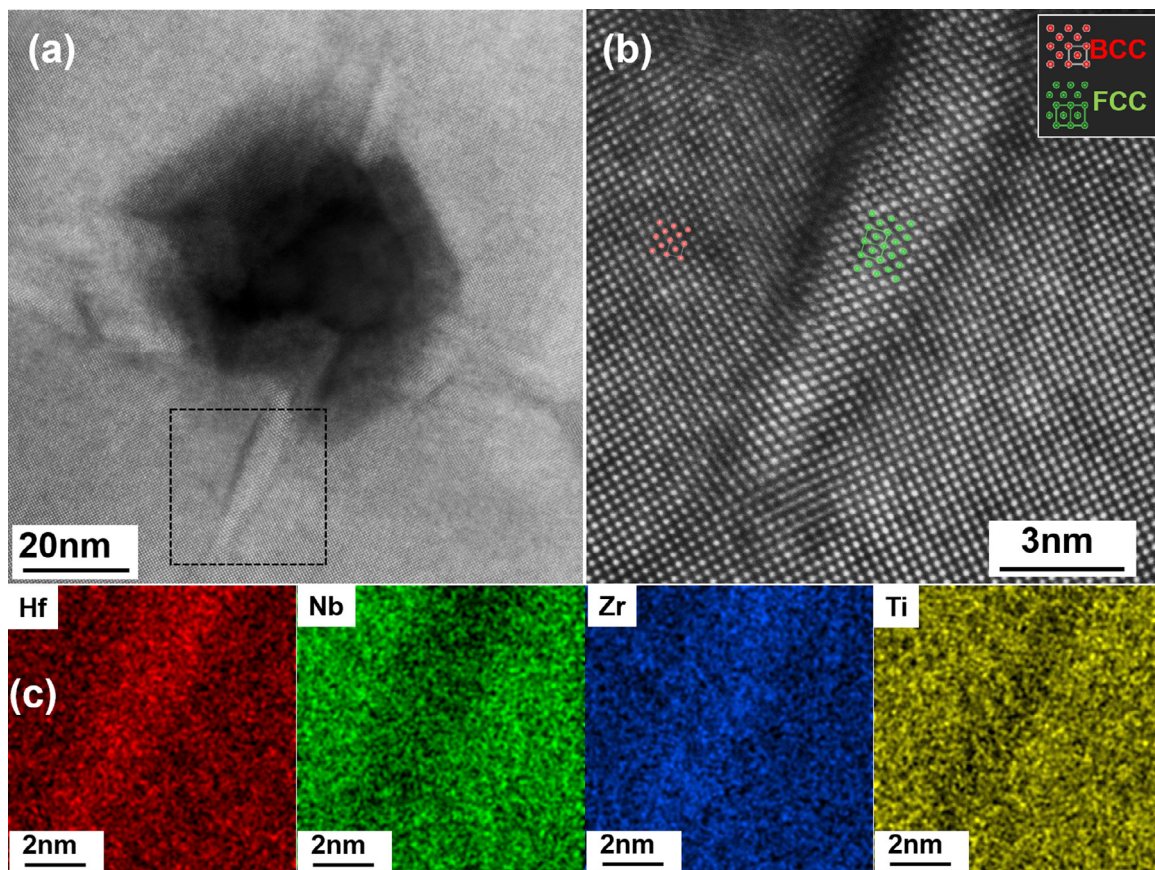


Fig. 5. STEM-HAADF images showing the (a) microstructure, (b) atomic-scale structure, and (c) EDS mapping of a cavity-precipitate complex formed under irradiation to the fluence of $5 \times 10^{16} \text{ cm}^{-2}$, through $<100>_{\text{BCC-matrix}}$. The overlayed red and green colored balls in (b) are the atomic structure models for $\{100\}_{\text{BCC}}$ and $\{110\}_{\text{FCC}}$ planes, respectively.

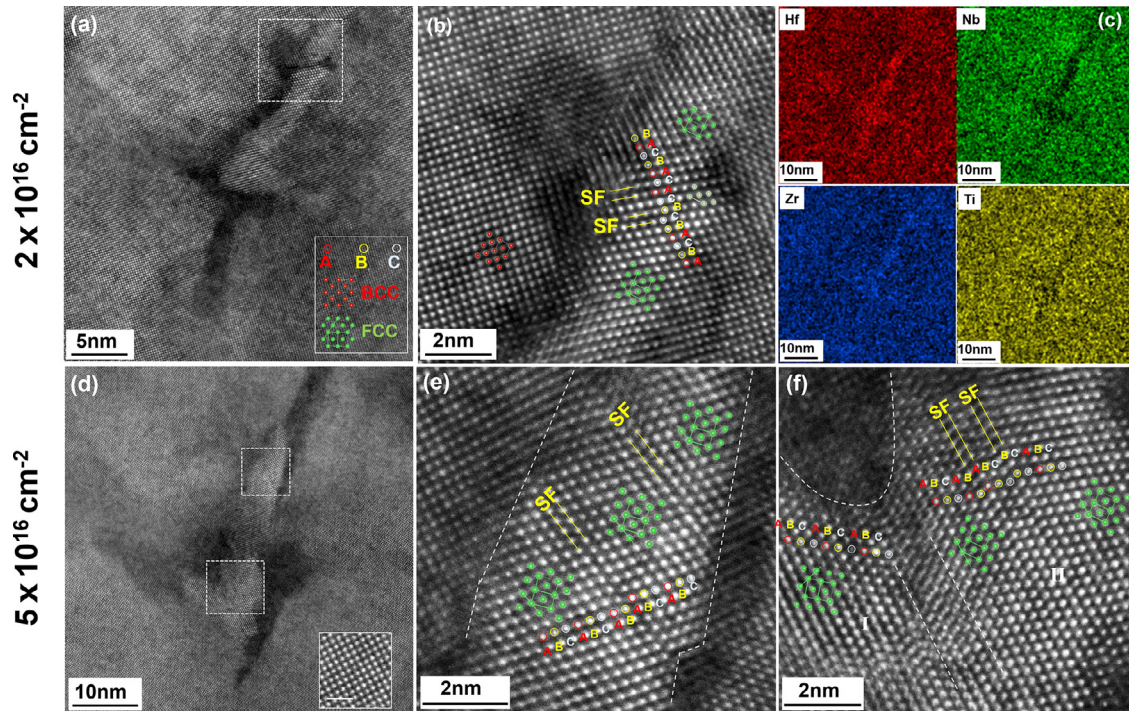


Fig. 6. STEM-HAADF images showing the (a, d) microstructure, (b, e, f) atomic-scale structure, and (c) EDS mapping of two precipitates formed under irradiation to the fluence of (a, b, c) $2 \times 10^{16} \text{ cm}^{-2}$ and (d, e, f) $5 \times 10^{15} \text{ cm}^{-2}$, through $<100>_{\text{BCC-matrix}}$. (b) corresponds to the dash square region in (a); (c) covers the entire precipitate in (a); (e) and (f) correspond to the top and bottom dash square regions in (d), respectively. The scale bar in the inset of (d) shows 1 nm. The overlaid red and green colored balls are the atomic structure models for $\{100\}_{\text{BCC}}$ and $\{110\}_{\text{FCC}}$ planes, respectively. The red, yellow, and gray circles indicate the A, B, and C stacking layers in the close-packed structure.

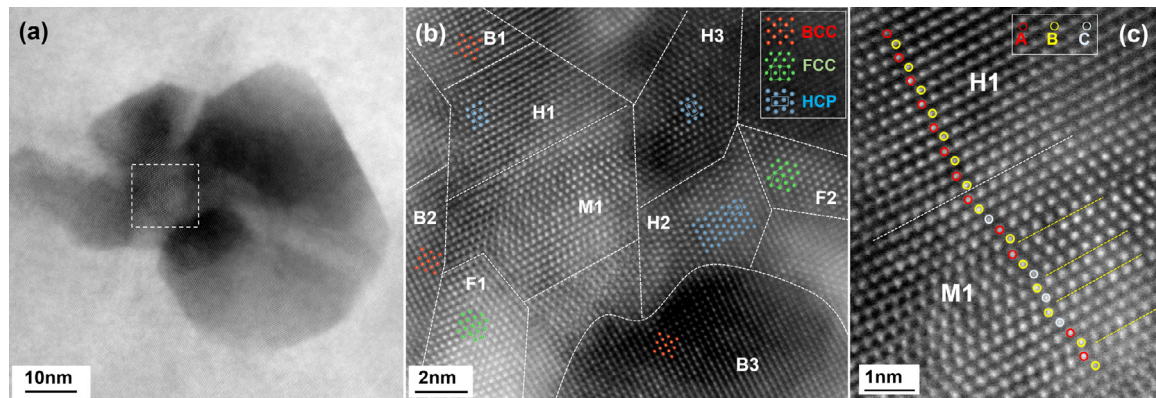


Fig. 7. STEM-HAADF images showing the (a) microstructure, (b, c) atomic-scale structure of a cavity-precipitate complex formed under irradiation to the fluence of $5 \times 10^{16} \text{ cm}^{-2}$, through $<100>_{\text{BCC-matrix}}$. The overlaid red, green, and blue colored balls are the atomic structure models for $\{100\}_{\text{BCC}}$, $\{110\}_{\text{FCC}}$, and $\{110\}_{\text{HCP}}$ planes, respectively. The red, yellow, and gray circles indicate the A, B, and C stacking layers in the close-packed structure.

especially those incoherent boundaries, may serve as the traps for irradiation-induced structural defects and implanted He atoms, which are likely to be responsible to the aggregation of vacancies and He atoms and promote the cavity formation.

Other than the structure of precipitates, the interfaces between the matrix and early-stage precipitates are examined to further understand the mechanism of precipitation. Overall speaking, two types of interfaces are observed in the present study. Fig. 8(a) shows the atomic-scale STEM-HAADF image of a first-type interfacial region, between a BCC phase and an FCC phase. Following the arrow from the top right to the bottom left direction (i.e., the $[00]_{\text{BCC}}$ direction), it can be clearly seen that the red square lattice on the $(100)_{\text{BCC}}$ plane in the BCC phase is gradually elongated in the $[0\bar{1}\bar{0}]$ direction, through a transition region (see the yellow rectangle), and eventually forms an FCC lattice (see the green rect-

angle on the $(110)_{\text{FCC}}$ plane). Note that this $(110)_{\text{FCC}}$ plane of the precipitate is parallel to the $(100)_{\text{BCC}}$ plane of the matrix, as evidenced by the fact that they are both perpendicular to the electron beam direction in Fig. 8(a). As illustrated in Fig. 8(c), the elongated $[010]_{\text{BCC}}$ vector is transformed into the $[001]_{\text{FCC}}$ vector, through which the projected atomic arrangement is described in Fig. 8(d). Considering that the interatomic distance in the FCC (and also HCP) structured Hf-Zr alloy, ~3.20 Å, is close to the lattice parameter of the BCC structured HfNbZrTi, ~3.44 Å [45], the lattice distortion within the $(010)_{\text{BCC}}/(001)_{\text{FCC}}$ planes is insignificant, which may reduce the energy barrier for such transition.

However, a large (~24%) lattice mismatch is brought in along the $[100]_{\text{BCC}}/[001]_{\text{FCC}}$ direction, as shown in Fig. 8(e), which may cause severe lattice distortion as demonstrated in Fig. 8(b). Following the red-green arrow, the cubic BCC lattice is elongated along

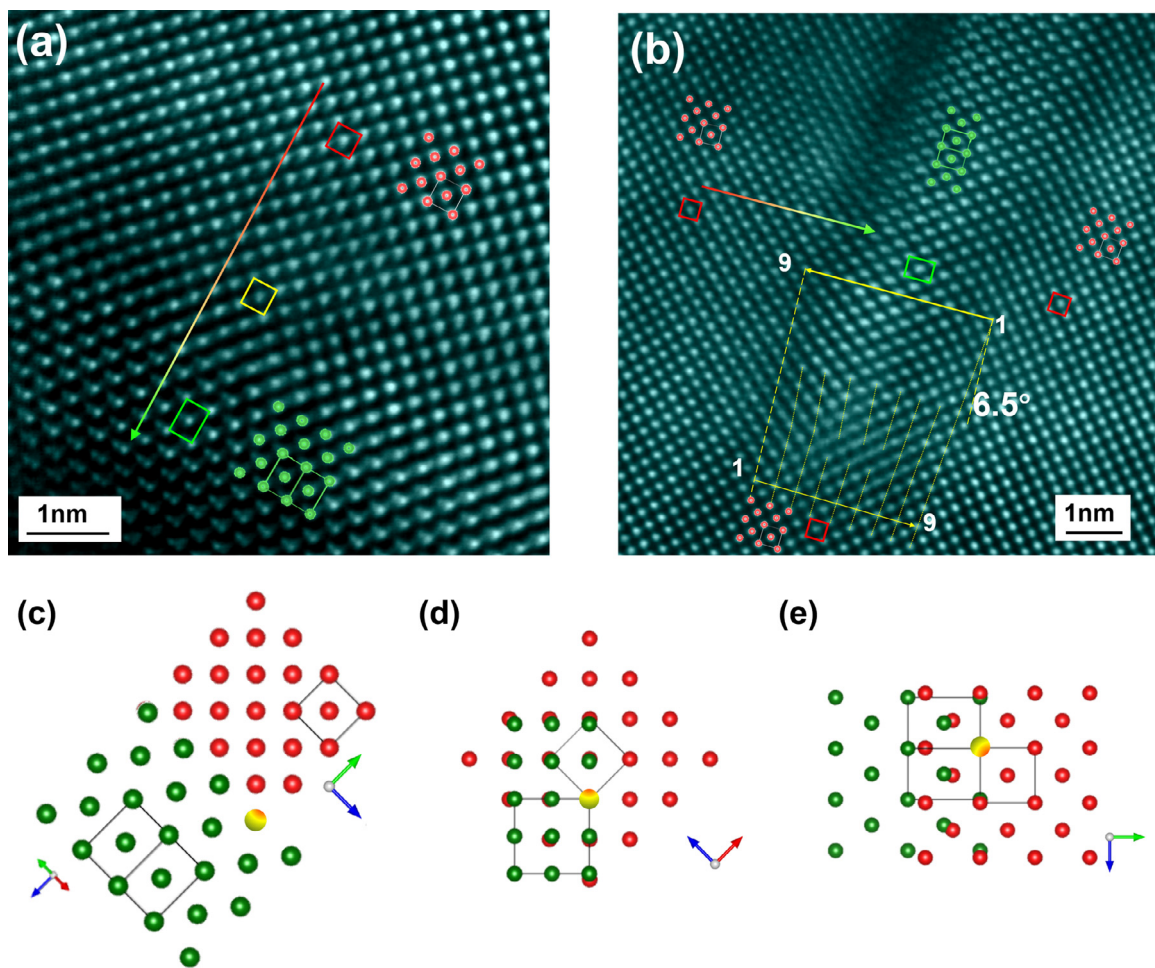


Fig. 8. (a, b) Wiener-filtered (using the Digital Micrograph software) STEM-HAADF images showing the interface regions of two precipitates. (b) is from a portion of Fig. 5(b). The marks in (a, b) are detailed in the main text. (c–e) show the atomic structural models, made with the VESTA software, for this type of interface. (d, e) illustrate the lattice mismatch between the two structures in different orientations. The atoms with gradient colors in (c–e) indicate the overlapping locations between the BCC and FCC lattices.

the $[0\bar{1}0]$ direction, and form an FCC structured phase, as marked with the green rectangle and the atomic structural model. This part of precipitate is surrounded by the BCC matrix from three directions (left, right, and bottom) in this image plane, and the interfacial region between the precipitate and the matrix to the bottom demonstrates a severe lattice distortion. It can be found by considering the yellow loop that, without any stacking fault or dislocation, the length of the top 9-atom row spanning the precipitate is ~16% longer than that at the bottom within the BCC matrix. One of the consequences is a misorientation of ~6.5° between the left and right regions of the BCC matrix, which is expected to cause structural instability leading to further phase evolution.

The other type of interface between the precipitates and the matrix observed in this study is shown in Fig. 9, between the BCC matrix and the HCP precipitates. As shown in Fig. 9(a), the HCP precipitate is located at the top right region, surrounded by the BCC matrix from the top left and the bottom directions. Other than the parallel relationship between the $(110)_{\text{HCP}}$ plane of the precipitate and the $(100)_{\text{BCC}}$ plane of the matrix, both of which are perpendicular to the electron beam direction, two other crystalline orientation relationships can also be identified. First, following the top arrow, it can be observed that the $[011]_{\text{BCC}}$ axis of the matrix is aligned with the $[001]_{\text{HCP}}$ axis of the precipitate. Second, following the bottom arrow, it can be observed that the $[0\bar{1}1]_{\text{BCC}}$ axis of the matrix is almost aligned with the $[1\bar{1}0]_{\text{HCP}}$ direction, but with slight lattice bending, due to the minor mismatch between

the length of the c axis in the HCP Hf-Zr structure (5.06 Å) and the face diagonal of the BCC HfNbZrTi (4.85 Å).

There has been a well-known Burgers path [46] proposed to describe the homogenous transition process from the BCC to HCP structured Zr. The orientation relationship shown in Fig. 9 is similar to that in the Burgers path, regarding the alignment between the $(001)_{\text{HCP}}$ and the $(110)_{\text{BCC}}$ (see Fig. 9 d). Nonetheless, in our case, the $[\pm 100]_{\text{BCC}}$ direction in the matrix is aligned with the $[110]_{\text{HCP}}$ direction, while in the Burgers path the $[11\bar{1}]_{\text{BCC}}$ direction is aligned with the $[0\bar{1}0]_{\text{HCP}}$ direction. In other words, there is an ~5° mismatch (between the blue and red dash lines in Fig. 9d) on the precipitate-matrix relative orientations between our observation and the Burgers path. Similarly, since the observed orientation relationship between the HCP and FCC structures are the same between this work and the Burgers path, which is naturally true since they are simply different in the stacking sequence, the relative orientations between the BCC and FCC structures also have an ~5° mismatch between the two studies. One possible reason for such discrepancy is that the Burgers path is for a homogeneous phase transition in elemental metals without compositional variation between the matrix and the precipitates, however, in our case the compositions are different, leading to different relationships regarding, e.g., lattice parameters, which are important for the lattice alignments. Here it must be noted that, it can hardly be certain that the orientation relationships from the Burgers path do not exist in our case, since it is impossible to screen every precipitate-

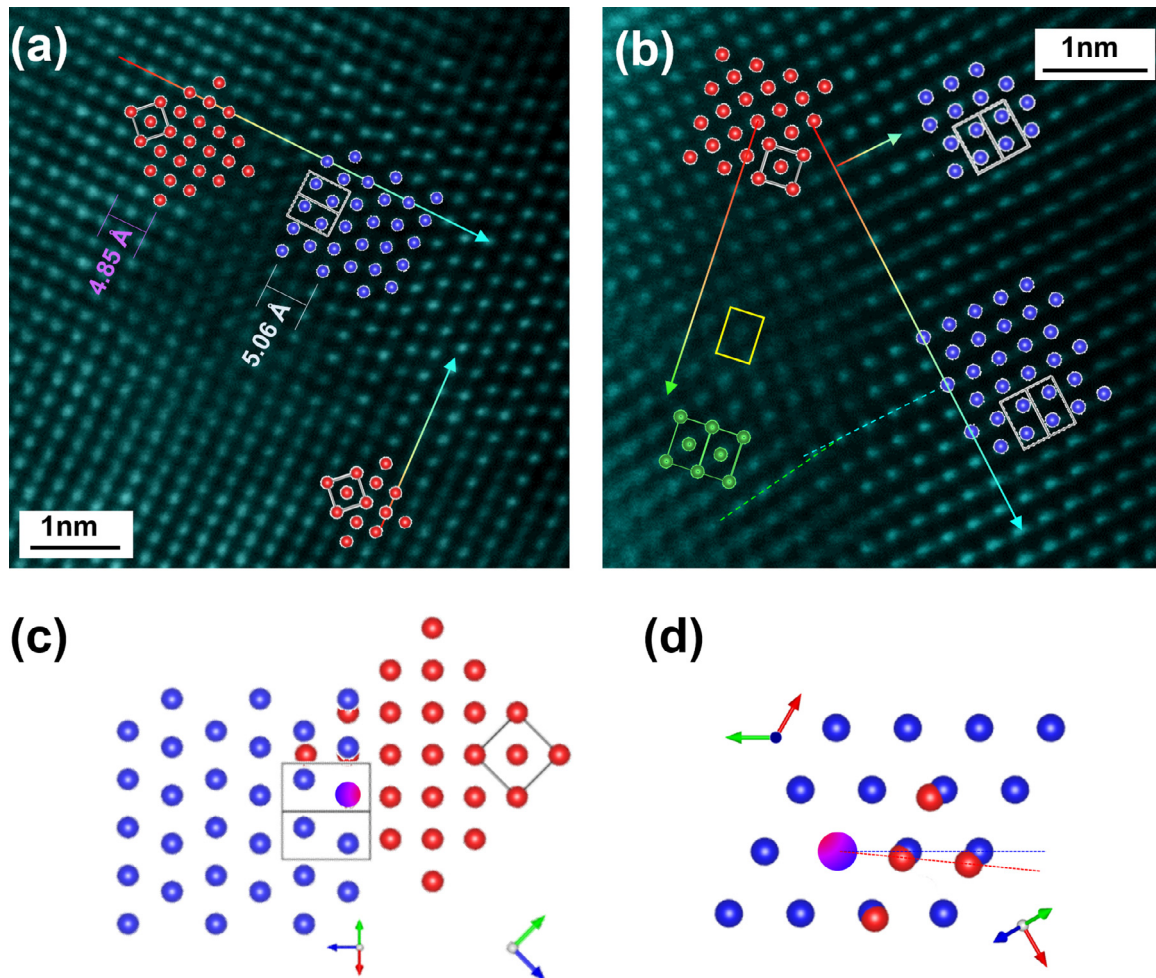


Fig. 9. (a, b) Wiener-filtered STEM-HAADF images showing the interface regions of two precipitates. (b) is from a portion of Fig. 7(b). The marks in (a, b) are detailed in the text. (c) and (d) show the atomic structural models viewed through different observation directions. The atoms with gradient colors in (c) and (d) indicate the overlapping locations between BCC and HCP lattices.

matrix interface. However, it is clear that different structural states can be at least metastable during the precipitation process.

Furthermore, it has been a long-term debate on whether or not intermediate FCC phases exist during the BCC-HCP phase transitions [47]. In the present work, both BCC-FCC and BCC-HCP interfaces are frequently observed between the matrix and early-stage precipitates with sizes of a few nanometers, while all the characterized extended precipitates are HCP structured. Moreover, as shown in Fig. 9 (b), one region of BCC matrix can transform into both FCC (following the left arrow) and HCP structured phase (following the middle and right arrows) along different directions. Furthermore, there exist many FCC precipitates with high density of stacking faults, as well as some precipitates with close-packed structures with highly mixed stacking sequences (see Fig. 7c). These results indicate that both the BCC-HCP path and the BCC-FCC-HCP path may occur simultaneously in HfNbZrTi under ion irradiation at elevated temperatures. Previous *ab-initio* calculations have reported lower but similar 0 K energies for the FCC structure of a specific RHEA composition compared with its HCP structure, to explain the observed FCC secondary phases formed during thermal annealing, indicating a compositional sensitive structural stability in RHEAs [48]. In our case, one of the possible reasons for the multiple structural transformation paths is the complex energy landscape of high entropy alloys, from both thermodynamic and kinetic perspectives [17, 49]. Such complexity may be further enhanced under irradiations at elevated temperatures due to local

elemental segregation, and results in the fluctuation of local structural preference.

4. Conclusions

In summary, the irradiation-enhanced precipitation and the impact on cavity formation have been investigated in a single-phase BCC structured refractory high entropy alloy, HfNbZrTi, under 1.5 MeV He ion irradiation at 700 °C, to the fluences of 5×10^{15} - 1×10^{17} cm $^{-2}$. The precipitation mechanisms have been discussed according to the atomic-scale structures and the orientation relationships observed at the interfaces between the matrix and precipitates. While chemically the precipitates are mostly Hf and Zr-enriched, structurally they can form through different paths. Other than the stabled HCP structure, both the FCC and the close-packed structures with highly mixed stacking sequences have been frequently observed in the early-stage precipitates with small sizes of a few nanometers, indicating the formation of intermediate phases during precipitation. Slightly different orientation relationships have been observed from the Burgers path, probably due to the variations in composition during precipitation. Unlike the previous studied HEAs under irradiation, the irradiation-enhanced precipitation in HfNbZrTi strongly affects the cavity formation, probably due to the very high density of phase/grain boundaries and the large lattice distortion that results from the precipitation process. The large but low density of cavities have

been observed to form through typical heterogeneous nucleation and growth mechanisms, accompanied by the precipitation process, and are highly clustered under high fluence irradiations. The present work has clearly demonstrated the significant impact of phase stability on the irradiation induced microstructural evolution, which should be carefully considered in the design of high entropy alloys for applications in nuclear engineering.

Declaration of Competing Interest

The authors declare that they have no known competing financial interests or personal relationships that could have appeared to influence the work reported in this paper.

CRediT authorship contribution statement

D. Li: Formal analysis, Investigation, Visualization, Writing - original draft, Writing - review & editing. **N. Jia:** Investigation. **H. Huang:** Investigation, Resources, Writing - review & editing. **S. Chen:** Investigation. **Y. Dou:** Investigation. **X. He:** Investigation. **W. Yang:** Conceptualization, Investigation, Resources. **Y. Xue:** Conceptualization, Investigation, Resources. **Z. Hua:** Investigation. **F. Zhang:** Investigation. **L. Wang:** Investigation. **K. Jin:** Conceptualization, Funding acquisition, Investigation, Project administration, Resources, Supervision, Writing - review & editing. **H. Cai:** Conceptualization, Resources, Supervision.

Acknowledgements

This work was supported by the [National Natural Science Foundation of China](#) (grant no. [11905008](#)) and a Continuous Support Project from the State Administration of Science, Technology and Industry for National Defense of China. KJ acknowledges the Analytical and Testing Center of Beijing Institute of Technology for assisting the TEM analyses.

Supplementary materials

Supplementary material associated with this article can be found, in the online version, at doi:[10.1016/j.jnucmat.2021.153023](https://doi.org/10.1016/j.jnucmat.2021.153023).

References

- [1] S.J. Zinkle, J.T. Busby, Structural materials for fission & fusion energy, Mater. Today 12 (11) (2009) 12–19.
- [2] J.W. Yeh, S.K. Chen, S.J. Lin, J.Y. Gan, T.S. Chin, T.T. Shun, C.H. Tsau, S.Y. Chang, Nanostructured high-entropy alloys with multiple principal elements: novel alloy design concepts and outcomes, Adv. Eng. Mater. 6 (5) (2004) 299–303.
- [3] B. Cantor, I.T.H. Chang, P. Knight, A.J.B. Vincent, Microstructural development in equiatomic multicomponent alloys, Mater. Sci. Eng. A 375–377 (2004) 213–218.
- [4] J.-W. Yeh, S.-J. Lin, Breakthrough applications of high-entropy materials, J. Mater. Res. 33 (19) (2018) 3129–3137.
- [5] S.J. Zinkle, Advanced Irradiation-Resistant Materials for Generation IV Nuclear Reactors, Structural Materials for Generation IV Nuclear Reactors, Elsevier Ltd, 2017.
- [6] N.A.P.K. Kumar, C. Li, K.J. Leonard, H. Bei, S.J. Zinkle, Microstructural stability and mechanical behavior of FeNiMnCr high entropy alloy under ion irradiation, Acta Mater. 113 (2016) 230–244.
- [7] Y. Zhang, G.M. Stocks, K. Jin, C. Lu, H. Bei, B.C. Sales, L. Wang, L.K. Beland, R.E. Stoller, G.D. Samolyuk, M. Caro, A. Caro, W.J. Weber, Influence of chemical disorder on energy dissipation and defect evolution in concentrated solid solution alloys, Nat. Commun. 6 (2015) 8736.
- [8] K. Jin, H. Bei, Y. Zhang, Ion irradiation induced defect evolution in Ni and Ni-based FCC equiatomic binary alloys, J. Nucl. Mater. 471 (2016) 193–199.
- [9] C. Lu, L. Niu, N. Chen, K. Jin, T. Yang, P. Xiu, Y. Zhang, F. Gao, H. Bei, S. Shi, M.-R. He, I.M. Robertson, W.J. Weber, L. Wang, Enhancing radiation tolerance by controlling defect mobility and migration pathways in multicomponent single-phase alloys, Nat. Commun. 7 (2016) 13564.
- [10] T.-n. Yang, C. Lu, G. Velisa, K. Jin, P. Xiu, M.L. Crespillo, Y. Zhang, H. Bei, L. Wang, Effect of alloying elements on defect evolution in Ni-20X binary alloys, Acta Mater. 151 (2018) 159–168.
- [11] X. Wang, K. Jin, D. Chen, H. Bei, Y. Wang, W.J. Weber, Y. Zhang, J. Poplawsky, K.L. More, Investigating effects of alloy chemical complexity on helium bubble formation by accurate segregation measurements using atom probe tomography, Microsc. Microanal. 25 (2019) 1558–1559.
- [12] D. Chen, S. Zhao, J. Sun, P. Tai, Y. Sheng, Y. Zhao, G. Yeli, W. Lin, S. Liu, W. Kai, J.-J. Kai, Diffusion controlled helium bubble formation resistance of FeCoNiCr high-entropy alloy in the half-melting temperature regime, J. Nucl. Mater. 526 (2019) 151747.
- [13] L. Yang, H. Ge, J. Zhang, T. Xiong, Q. Jin, Y. Zhou, X. Shao, B. Zhang, Z. Zhu, S. Zheng, X. Ma, High He-ion irradiation resistance of CrMnFeCoNi high-entropy alloy revealed by comparison study with Ni and 304SS, J. Mater. Sci. Technol. 35 (2019) 300–305.
- [14] K. Jin, C. Lu, L.M. Wang, J. Qu, W.J. Weber, Y. Zhang, H. Bei, Effects of compositional complexity on the ion-irradiation induced swelling and hardening in Ni-containing equiatomic alloys, Scr. Mater. 119 (2016) 65–70.
- [15] K. Jin, H. Bei, Single-phase concentrated solid-solution alloys: bridging intrinsic transport properties and irradiation resistance, Front. Mater. 5 (2018).
- [16] Y. Zhang, K. Jin, H. Xue, C. Lu, R.J. Olsen, L.K. Beland, M.W. Ullah, S. Zhao, H. Bei, D.S. Aidhy, G.D. Samolyuk, L. Wang, M. Caro, A. Caro, G.M. Stocks, B.C. Larson, I.M. Robertson, A.A. Correa, W.J. Weber, Influence of chemical disorder on energy dissipation and defect evolution in advanced alloys, J. Mater. Res. 31 (16) (2016) 2363–2375.
- [17] Y. Zhang, S. Zhao, W.J. Weber, K. Nordlund, F. Granberg, F. Djurabekova, Atomic-level heterogeneity and defect dynamics in concentrated solid-solution alloys, Curr. Opin. Solid State Mater. Sci. 21 (5) (2017) 221–237.
- [18] D.B. Miracle, O.N. Senkov, A critical review of high entropy alloys and related concepts, Acta Mater. 122 (2017) 448–511.
- [19] C. Lu, T. Yang, K. Jin, N. Gao, P. Xiu, Y. Zhang, F. Gao, H. Bei, W.J. Weber, K. Sun, Y. Dong, L. Wang, Radiation-induced segregation on defect clusters in single-phase concentrated solid-solution alloys, Acta Mater. 127 (2017) 98–107.
- [20] M.-R. He, S. Wang, S. Shi, K. Jin, H. Bei, K. Yasuda, S. Matsumura, K. Higashida, I.M. Robertson, Mechanisms of radiation-induced segregation in Cr-FeCoNi-based single-phase concentrated solid solution alloys, Acta Mater. 126 (2017) 182–193.
- [21] B. Kombaiah, K. Jin, H. Bei, P.D. Edmondson, Y. Zhang, Phase stability of single phase Al0.12CrNiFeCo high entropy alloy upon irradiation, Mater. Des. 160 (2018) 1208–1216.
- [22] D.J.M. King, S.T.Y. Cheung, S.A. Humphrey-Baker, C. Parkin, A. Couet, M.B. Cortie, G.R. Lumpkin, S.C. Middleburgh, A.J. Knowles, High temperature, low neutron cross-section high-entropy alloys in the Nb-Ti-V-Zr system, Acta Mater. 166 (2019) 435–446.
- [23] O. El-Atwani, N. Li, M. Li, A. Devaraj, J.K.S. Baldwin, M.M. Schneider, D. Sobieraj, J.S. Wrobel, D. Nguyen-Manh, S.A. Maloy, E. Martinez, Outstanding radiation resistance of tungsten-based high-entropy alloys, Sci. Adv. 5 (3) (2019) eaav2002.
- [24] G.S. Was, Fundamentals of Radiation Materials Science: Metals and Alloys, Springer, Berlin, Heidelberg, New York, 2007.
- [25] W. Kesternich, Helium trapping at dislocations, precipitates and grain boundaries, Radiat. Effects 78 (1–4) (1983) 261–273.
- [26] A.D. Braillsford, L.K. Mansur, The effect of precipitate-matrix interface sinks on the growth of voids in the matrix, J. Nucl. Mater. 104 (1981) 1403–1408.
- [27] S. Ukai, M. Fujiwara, Perspective of ODS alloys application in nuclear environments, J. Nucl. Mater. 307–311 (2002) 749–757.
- [28] A. Ayyagari, R. Salloum, S. Muskeri, S. Mukherjee, Low activation high entropy alloys for next generation nuclear applications, Materialia 4 (2018) 99–103.
- [29] A. Kareer, J.C. Waite, B. Li, A. Couet, D.E.J. Armstrong, A.J. Wilkinson, Short communication: 'low activation, refractory, high entropy alloys for nuclear applications, J. Nucl. Mater. 526 (2019) 151744.
- [30] N. Jia, Y. Li, X. Liu, Y. Zheng, B. Wang, J. Wang, Y. Xue, K. Jin, Thermal stability and mechanical properties of low-activation single-phase Ti-V-Ta medium entropy alloys, JOM 71 (10) (2019) 3490–3498.
- [31] Y.D. Wu, Y.H. Cai, T. Wang, J.J. Si, J. Zhu, Y.D. Wang, X.D. Hui, A refractory Hf25Nb25Ti25Zr25 high-entropy alloy with excellent structural stability and tensile properties, Mater. Lett. 130 (2014) 277–280.
- [32] Y.X. Ye, C.Z. Liu, H. Wang, T.G. Nieh, Friction and wear behavior of a single-phase equiatomic TiZrHfNb high-entropy alloy studied using a nanoscratching technique, Acta Mater. 147 (2018) 78–89.
- [33] W. Li, D. Xie, D. Li, Y. Zhang, Y. Gao, P.K. Liaw, Mechanical behavior of high-entropy alloys, Progr. Mater. Sci. (2021).
- [34] Z. Lei, X. Liu, Y. Wu, H. Wang, S. Jiang, S. Wang, X. Hui, Y. Wu, B. Gault, P. Konitis, D. Raabe, L. Gu, Q. Zhang, H. Chen, H. Wang, J. Liu, K. An, Q. Zeng, T.G. Nieh, Z. Lu, Enhanced strength and ductility in a high-entropy alloy via ordered oxygen complexes, Nature 563 (7732) (2018) 546–550.
- [35] S.J. Zinkle, G.S. Was, Materials challenges in nuclear energy, Acta Mater. 61 (3) (2013) 735–758.
- [36] J.F. Ziegler, J.P. Biersack, M.D. Ziegler, SRIM—the Stopping and Range of Ions in Solids, SRIM Co., Chester, MD, 2008.
- [37] M. Moschetti, A. Xu, B. Schuh, A. Hohenwarter, J.-P. Couzinie, J.J. Krizic, D. Bhattacharyya, B. Gludavatz, On the room-temperature mechanical properties of an ion-irradiated TiZrNbHfTa refractory high entropy alloy, JOM 72 (2019) 130–138.
- [38] Y. Ma, S. Wu, Y. Jia, P. Hu, Y. Bu, X. Chen, G. Wang, J. Liu, H. Wang, Q. Zhai, Hexagonal closed-packed precipitation enhancement in a NbTiHfZr refractory high-entropy alloy, Metals 9 (5) (2019).

- [39] O.N. Senkov, J.M. Scott, S.V. Senkova, D.B. Miracle, C.F. Woodward, Microstructure and room temperature properties of a high-entropy TaNbHfZrTi alloy, *J. Alloys Compd.* 509 (20) (2011) 6043–6048.
- [40] A. Takeuchi, A. Inoue, Classification of bulk metallic glasses by atomic size difference, heat of mixing and period of constituent elements and its application to characterization of the main alloying element, *Mater. Trans.* 46 (2005) 2817–2829 JIM.
- [41] F. Otto, Y. Yang, H. Bei, E.P. George, Relative effects of enthalpy and entropy on the phase stability of equiatomic high-entropy alloys, *Acta Mater.* 61 (7) (2013) 2628–2638.
- [42] Y. Li, L. Wang, G. Ran, Y. Yuan, L. Wu, X. Liu, X. Qiu, Z. Sun, Y. Ding, Q. Han, X. Wu, H. Deng, X. Huang, In-situ TEM investigation of 30 keV He⁺ irradiated tungsten: effects of temperature, fluence, and sample thickness on dislocation loop evolution, *Acta Mater.* (2021) 206.
- [43] Y. Li, G. Ran, Y. Guo, Z. Sun, X. Liu, Y. Li, X. Qiu, Y. Xin, The evolution of dislocation loop and its interaction with pre-existing dislocation in He⁺-irradiated molybdenum: in-situ TEM observation and molecular dynamics simulation, *Acta Mater.* 201 (2020) 462–476.
- [44] N. Jia, Y. Li, H. Huang, S. Chen, D. Li, Y. Dou, X. He, W. Yang, Y. Xue, K. Jin, Helium bubble formation in refractory single-phase concentrated solid solution alloys under MeV He ion irradiation, *J. Nucl. Mater.* (2021) 550.
- [45] Y. Tong, S. Zhao, H. Bei, T. Egami, Y. Zhang, F. Zhang, Severe local lattice distortion in Zr- and/or Hf-containing refractory multi-principal element alloys, *Acta Mater.* 183 (2020) 172–181.
- [46] W.G. Burgers, On the process of transition of the cubic-body-centered modification into the hexagonal-close-packed modification of zirconium, *Physica* 1 (7–12) (1934) 561–586.
- [47] Z. Lu, W. Zhu, T. Lu, W. Wang, Does the fcc phase exist in the Fe bcc–hcp transition? A conclusion from first-principles studies, *Model Simul. Mater. Sc.* 22 (2) (2014).
- [48] M. Heidelmann, M. Feuerbacher, D. Ma, B. Grabowski, Structural anomaly in the high-entropy alloy ZrNbTiHf, *Intermetallics* 68 (2016) 11–15.
- [49] S. Zhao, G.M. Stocks, Y. Zhang, Defect energetics of concentrated solid-solution alloys from ab initio calculations: Ni0.5Co0.5, Ni0.5Fe0.5, Ni0.8Fe0.2 and Ni0.8Cr0.2, *Phys. Chem. Chem. Phys.* 18 (34) (2016) 24043–24056.